

**Herbert Oertel
Kathrin Spiegel
Sven Donisi**

Modelling the Human Cardiac Fluid Mechanics

2nd edition



universitätsverlag karlsruhe

Herbert Oertel
Kathrin Spiegel
Sven Donisi

**Modelling the Human
Cardiac Fluid Mechanics**

2nd edition

Modelling the Human Cardiac Fluid Mechanics

von

Herbert Oertel
Kathrin Spiegel
Sven Donisi

2nd edition



universitätsverlag karlsruhe

Autoren

Prof. Prof. e.h. Dr.-Ing. habil. Herbert Oertel, Ordinarius
Dipl.-Ing. Kathrin Spiegel
Dr. Ing. Sven Donisi

Institut für Strömungslehre, Universität Karlsruhe (TH)
Kaiserstr. 12, 76128 Karlsruhe

2nd edition

Impressum

Universitätsverlag Karlsruhe
c/o Universitätsbibliothek
Straße am Forum 2
D-76131 Karlsruhe
www.uvka.de



Dieses Werk ist unter folgender Creative Commons-Lizenz
lizenziert: <http://creativecommons.org/licenses/by-nc-nd/2.0/de/>

Universitätsverlag Karlsruhe 2006
Print on Demand

ISBN-13: 978-3-86644-087-6
ISBN-10: 3-86644-087-1

Modelling the Human Cardiac Fluid Mechanics

H. Oertel^{*}, K. Spiegel, S. Donisi

Institute for Fluid Mechanics, University of Karlsruhe, D-76128 Karlsruhe, Germany

Abstract

In the second edition of the article a virtual heart model simulating the flow in the active left human ventricle and atrium is presented. Because in vivo myocardium data is not available, the movement of the active ventricle and its atrium is given by three-dimensional, time-dependent in vivo image data of a nuclear spin MRI tomograph. The passive part of the virtual heart model consists of a model aorta and of two-dimensionally modelled heart valves. As the flow is actively driven by the ventricle and atrium, a coupling of flow and structure is necessary to take into account the deviation of the aorta and the closing and opening of the heart valves. This coupling is replaced by the movement given by MRI tomograph and ultrasonic Doppler echocardiography, since we focus on the flow simulation in the left pumping ventricle.

The flow simulation is performed by a validated commercial software package that uses the finite volume method. The flow resistance of the circulation through the body is taken into account with a simplified circulation model.

The article shows how the virtual heart model can be used to predict flow losses and flow structures due to pathological ventricle contraction defects. It provides as an example the flow simulation of an unhealthy human ventricle with an aneurysm. The flow structure and flow losses are considered before and after surgery.

^{*}

Email address: oertel@isl.mach.uni-karlsruhe.de (H. Oertel).
URL: www-isl.mach.uni-karlsruhe.de (H. Oertel).

1 Introduction

To predict the flow in the human heart, we need to model the time-dependent geometry of the ventricle, the atrium and the heart valves during one cardiac cycle. In literature many approaches to model the electro-mechanical pump behavior of the heart are found (Fung (1997)). The structure of the muscle fibers of the human heart has already been published by Robb and Robb (1942). Hunter et al. (1996), (1998), Nash and Hunter (2000) developed a finite elasticity theory and a finite element method for analyzing ventricular electro-mechanics during the filling phase of the cardiac cycle, when cardiac muscle cells are not actively contracting. The orthotropic properties of the passive tissue are described by a constitutive law whose parameters are derived from a model of collagen fibers and in vitro stress measurements on animal hearts. A model of the active tissue properties, based on isolated animal muscle experiments, is also introduced in order to predict distributions of principal strain at the end of the contraction phase of the cardiac cycle. The mathematical modelling of the electrical activity of the heart has been summarized in the book by Pullan et. al (2005).

The calculation of the flow-structure coupling of the heart was introduced by Peskin and McQueen (1997), (2001). It approximates the muscle fibers of the heart as well as the cardiac valves in the Lagrangian description by considering discrete elastic fiber filaments embedded in the flow. The discretization of the fiber filaments is chosen to be so fine that they have no volume or mass, but can still be used for a continuum mechanical description of the material. At each point of the filament-flow combination, a unique fiber direction is given. The degree of detail of the model structure is very high, and in particular the structure of the heart valves is modelled very precisely. The method was further developed by Lemmon and Yoganathan (2000), and applied with a simplified model to the left ventricle of the heart for the filling phase of the cardiac cycle. Watanabe et al. (2002), (2004) chooses another approach to the flow-structure coupling of the heart, based on a simplified electro-physical and muscle contraction model. The coupling of the flow with the mechanical structure model of the cardiac muscle takes place via the pressure.

All these ventricular flow simulations are based on myocardium models of in vitro animal hearts or of simplified tissue modelling. Therefore, the results are not transferrable to the living human heart. With the experimentally validated Karlsruhe Heart Model (KAHMO), we present a time-dependent left ventricular geometrical model for a complete cardiac cycle (Oertel (2004), (2005), Schenkel et. al (2007)). It is based on patient-specific nuclear spin tomography MRI image data. The averaged inflow and outflow rates through the valves are adapted to magnetic resonance flux measurements.

The method used for the KAHMO ventricle model is independent of but similar in approach to those presented by Jones et al. (1998), Baccani et al. (2002), (2003) and Saber et. al (2001), (2003), who define the boundary configuration for a flow model for the left ventricle. Nakamura et. al (2003) presented a similar approach on the basis of velocity measurements during the filling of the ventricle made with Doppler CMD- echocardiography. The determination of three-dimensional velocity fields in the ventricular long axis plane has also been carried out by Houlind et al. (1994), Kim et. al (1995), Kilner et al. (2000) and Long et al. (2003). Furthermore, Kim et. al (1995) quantified the left ventricle vortex seen during diastole. Walker et. al (1996) measured the three-dimensional velocity field in multiple slices in the human heart. Pedrizzetti and Domenichini (2005), showed that the inlet jet generates a ring vortex behind the annular orifice of the mitral valve. Due to lateral displacement of the valve from the ventricle axis and the movement of the myocardium, the vortex grows asymmetrically in time. This vertebration during diastole is described correctly in most of the papers. Yet, none of them mention from a topological point of view the three-dimensional saddle-foci bifurcation in the apex of the ventricle that derives from the asymmetrical vortex ring. This bifurcation influences the time sequence of the outflow jet through the aortic valve at systole. It is one of the topics of this article. The flow topology has been investigated in four MRI data sets of healthy human hearts. One of them is described in detail and acts as reference for flow simulations of a human aneurysm ventricle defect. The article shows patient-specific simulation results before and after surgery and furthermore the potential of application in clinical use.

1.1 *The Human Heart*

The human heart (Fig. 1) is a four chambered muscular organ that contracts and expands periodically while pumping 4 to 5 l per minute of blood into circulation. Returning from systemic circulation, oxygen-poor blood enters the right atrium and is passed on to the right ventricle to be delivered by contraction into pulmonary circulation. The reoxygenated blood returns to the left atrium and is passed through the left ventricle into systemic circulation. To ensure that blood flows only one way and that the atria can be filled during contraction, four valves regulate the blood flow. These are located between the right atrium and right ventricle (*tricuspid valve*), between the right ventricle and pulmonary artery (*pulmonary valve*), between the left atrium and left ventricle (*mitral valve*) and between the left ventricle and aorta (*aortic valve*), respectively. Each valve has a set of flaps that open in only one direction due to pressure. The mitral valve has two flaps, while the others have three.

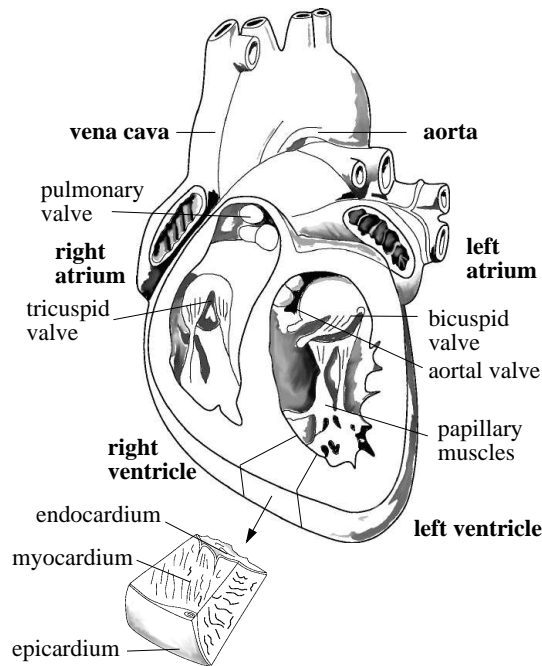


Fig. 1. Human heart

A pump cycle (Fig. 2) is associated with changes in ventricular and arterial pressure, shown in Figure 3. As shown in the pressure-volume diagram, the cycle can be split into filling (1), isovolumetric contraction (2), expulsion (3) and isovolumetric relaxation (4). Phases (2) and (3) are known as *systole*, while phases (4) and (1) describe the *diastole*.

Due to slightly higher pressure in the left atrium than in the left ventricle, the mitral valve is open during the filling phase (1). While the ventricle expands and its pressure increases, the aortal pressure decreases continuously, corresponding with the blood flow in the arterial vascular system, but it still remains high enough that the aortic valve remains closed. With the start of contraction (phase 2), the ventricle pressure exceeds the atrium pressure, and as a consequence, the mitral valve closes. With both valves closed, isovolumetric contraction increases the ventricle pressure up to 166 mbar, which exceeds the aortal pressure and forces the aortic valve open. Now, a constant volume of 80 ml blood flows out into the aorta while pressure increases from its minimum value of 107 mbar to its maximum of 160 mbar. Due to relaxation (phase 3) the ventricle pressure drops again below aortal pressure, and the aortic valve closes. Isovolumetric relaxation follows until the ventricle pressure is below the atrium pressure. The mitral valve opens and the cardiac cycle starts again. The pressure-volume diagram in Figure 3 shows the filling of the left ventricle.

The mechanical contraction of the cardiac muscle is controlled by periodic electrical impulses, that start with the excitation of the sinoatrial node. In

its function as primary pace maker, the sinoatrial node sends cyclical electrical depolarization and polarization. During the depolarization phase, the discharge extends across the conduction paths with a velocity of 1 m/s into the surrounding muscles of the atria, which then contract. The electrical impulse of the sinoatrial node is delayed in the ventricular node. This delay permits optimal filling of the ventricles during contraction of the atria. The impulse passes along the His nerve fibers and the sides of the chamber with a velocity of 1–4 m/s and reaches the ventricle muscles after about 110 ms. In the direction of the ventricle, the bundle of His divides into the left and right sides of the chamber.

As the ventricles begin to contract, the contraction in the atria ends, thanks to the delay of the conduction in the ventricular nodes. At this point all nerve cells in the impulse conduction system, apart from the impulse-forming cells in the sinoatrial nodes and ventricular nodes, can be spontaneously depolarized. The ventricular depolarization in the electrocardiogram in Figure 3 takes less than 0.1 s.

The cycle of depolarization and polarization generates a small electrical potential which can be measured on the surface of the body. The depolarization of the atria causes a small deflection, called the P-wave. After a pause of less than 0.2 s, this is followed by a strong deflection due to the depolarization of both ventricles (QRS). The T-wave then follows, caused by renewed polarization of the ventricles. The association of the electrical potentials with the mechanical processes and pressure changes in the left ventricle of the heart is

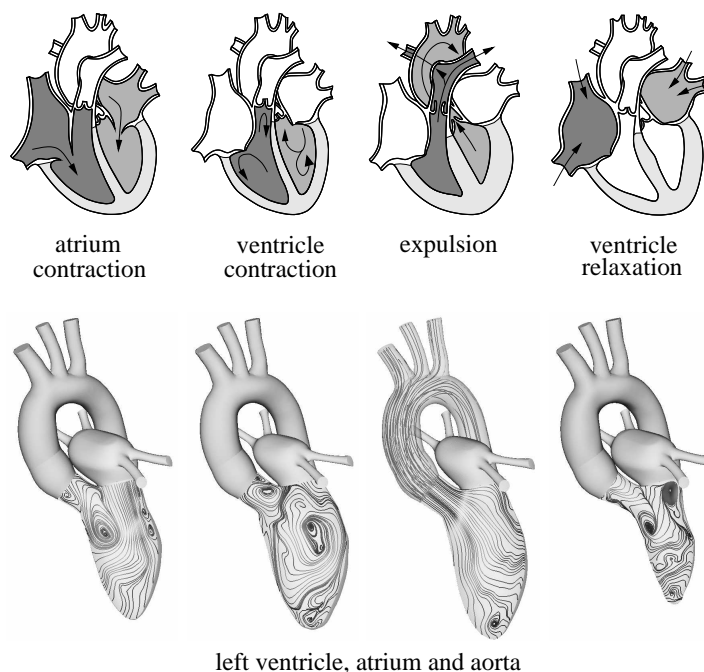


Fig. 2. Four phases of cardiac cycle

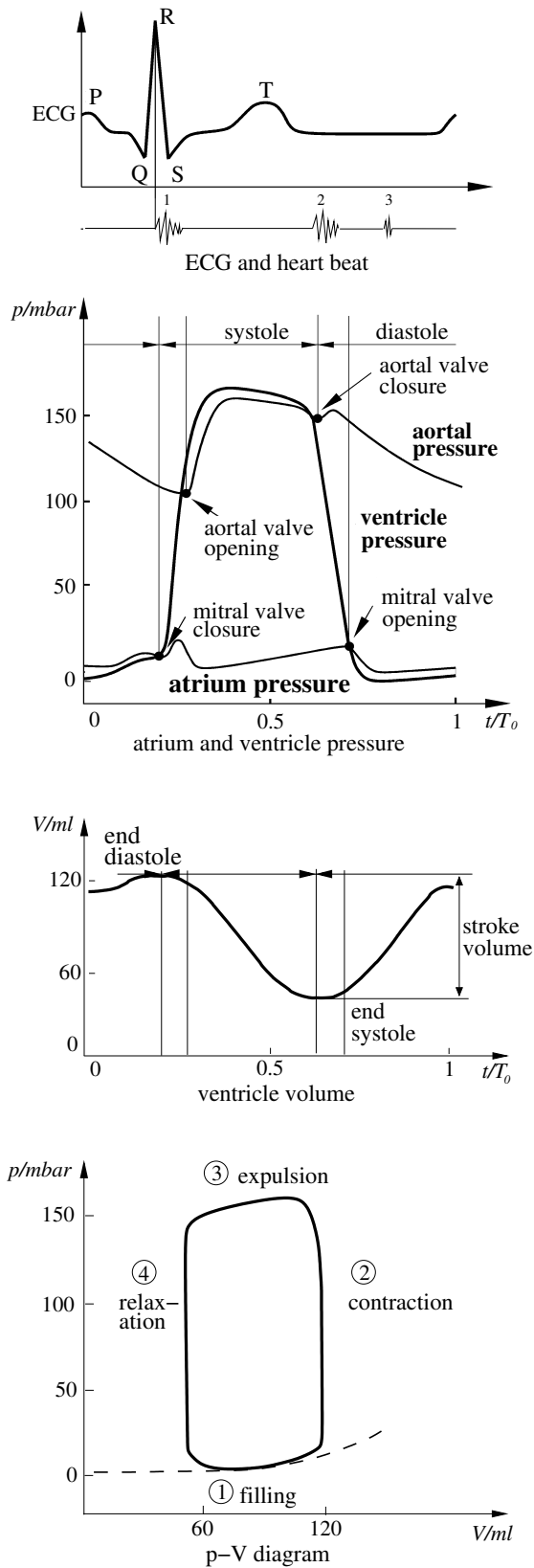


Fig. 3. Sketch of Electrocardiogram (ECG), pressure and volume in the left ventricle, cardiac cycle $T_0 = 0.8$ s

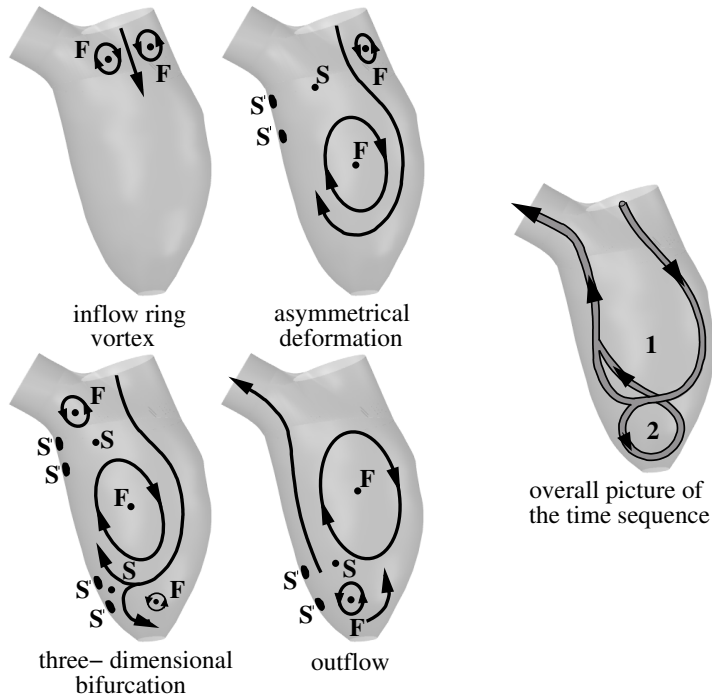


Fig. 4. Cardiac flow in the left ventricle

also shown in Figure 3.

As the mitral valve closes, the pressure in the left ventricle rises. This is associated with a sound wave which is detected as the first heart beat. This induces the systole, the phase of ventricle contraction. At the second heart beat, the aortal valve closes and the phase of ventricle relaxation begins. The third heart beat emanates from the sound wave of the filling process.

Figure 4 describes the directions of flow in the ventricle by summarizing the flow pictures shown in Figure 2. In reference to Figure 3, the mitral valve opens at $t/T_0 = 0.76$ of the cardiac cycle for the simulation parameters of Section 3. The filling process starts with an intake jet that is slowed down in the blood at rest. Due to high differences in velocities, the jet is accompanied by a ring vortex that expands and deforms three-dimensionally during the diastole because of the movement of the myocardium. The foci and saddle points of flow topology are sketched in the long axis plane. As shown in Figure 4, the ring vortex branches after about $t/T_0 = 0.29$ and moves towards the aortic valve (1). Blood washes through the apex of the ventricle (2). The velocity of the now three-dimensionally branched flow decreases until the intake flow process is completed with the closing of the mitral valve. Further three-dimensional deformation of the vortex structure is caused by flow inertia. With the opening of the aortic valve at $t/T_0 = 0.37$, a jet flow forms in the aorta, washing out the main flow (1) and later flow (2). As a result, the vortex structure is completely separated at the end of the systole. The healthy heart expels 63% of the ventricular volume during one cardiac cycle. Total expulsion and blood

exchange take place over two to three cardiac cycles.

The ventricular flow structure of Figure 4 is controversially discussed in literature. Reul et al. (1981) and Nakamura et. al (2003) show a stagnation point in the flow with a slightly asymmetrical ring vortex during diastole. This flow is not relevant for a cyclical, three-dimensional flow behavior in a human ventricle. Kilner et al. (2000) and (2004) describe the asymmetrical growth of the inflow ring vortex at late diastole, that forms a clockwise vortex in the long axis plane. None of them mention the three-dimensional bifurcation in the apex of the ventricle, sketched in Figure 4. Oertel (2005) discusses a counter clockwise vortex in the long axis plane, which is from a topological point of view also a possible flow configuration. Further flow simulations have shown, that this three-dimensional configuration only forms if the mitral valve axis is inclined. So far the mitral valve position is a very sensitive parameter for ventricular flow simulations.

1.2 Blood Circulation

The *systemic circulation* can be split into three main parts, the blood distribution system, consisting of the *aorta*, large and small *arteries* and *arterioles*. These further divide into the *capillaries*, where gas and material exchange takes place in the micro-circulation by diffusion. The blood flows back to the heart via the *venules*, small and large *veins* and the *vena cava*.

The mean blood pressure on leaving the left ventricle is about 133 mbar. This drops to 13 mbar when the blood returns to the right ventricle. Figure 5 shows the mean pressure and pressure variations in the different artery regimes. Because of the elastic properties of the aorta, the pressure pulses between 120 mbar and 160 mbar around the mean value. In the large arteries, the amplitude of the pulsation initially increases, because of the wave reflection.

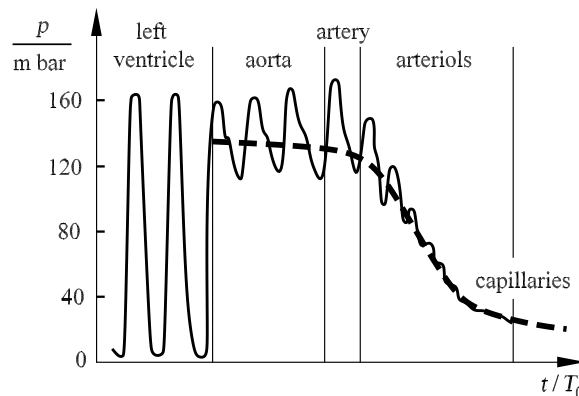


Fig. 5. Pressure in the arterial circulation

It then sinks drastically to a mean value of 40 mbar in the arteriole region over a distance of a few millimeters. In the capillaries and venules, the pressure drop continues less sharply. Eventually, there is a pressure of 13 mbar to push the blood back to the right ventricle. In the large veins and the vena cava, there is no pulse and no considerable pressure drop. Simultaneous pressure waves occur which are due to the pulsation of the right ventricle and move in the opposite direction to the flow of blood. The systolic pressure in the pulmonary arteries is quite small, about 20 mbar. A pressure drop of only 13 to 7 mbar is needed in order to overcome the flow drag in the lung volume, and so 13 to 7 mbar filling pressure remain for the left ventricle.

Because of their elasticity, the aorta and the large arteries act as a so-called *volume reservoir*. The acceleration part of the blood pulse is reduced and a higher pressure level is retained during the diastole and systole. This means that the flow in the arterial branches is smoother.

Between each pressure pulse, the arteries contract by about 5% and so maintain the blood transport. The pressure pulse in the arteries is positive, even during the systole of the heart. In contrast, a backflow occurs in the large arteries for a short time. The flow velocity is zero as the aortic valve is closed. The amplitude of the flow pulse decreases with increasing arterial branches and the pulse width increases while a smaller backflow occurs. The forward motion of the pressure pulse through the arterial branches is initially associated with an increase in the pressure amplitude, which is caused by the arterial branches and also by the decrease in elasticity of the artery wall. The flow profile in the branched arteries becomes more uniform.

The Reynolds numbers formed with the mean velocity are 3700 for the aorta, 500 for the large arteries, 0.7 for the arterioles, $2 \cdot 10^{-3}$ in the capillaries, 0.01 in the venules, 140 in the large veins and 3300 in the vena cava. The beating of the heart causes a periodic laminar flow in the smaller arteries and a transitional flow in the larger arteries and the aorta. The transition to turbulent flow takes place over a short time in the turning points of the velocity profile, close to the walls of the arteries. However, because of the shortness of the flow pulse the local transition to turbulence in the wall boundary layer cannot take place completely.

In the curved arteries and in particular in the aorta, the centrifugal force causes *secondary flows*. These have a velocity component perpendicular to the streamlines and cause a circulation flow in the direction of the outer wall. Figure 6 shows a snapshot of the velocity distribution and flow simulation in the bend of the aorta taking into account the centrifugal force, the streamline branching in the head, leg and collarbone arteries, and the flow structure of the secondary flow in the descending aorta. At the beginning of the systole, the flow first reaches a maximum at the inner side of the ascending aorta.

After passing through the curved and branching region, the velocity maximum moves to the outer side of the aorta curve. Because of the centrifugal force, two secondary vortices arise which remain well into the diastole. Half-way through the cardiac cycle a radial evasive motion of the aorta can be observed. The point of maximum deceleration of the flow is passed through. The velocity profile then flattens and a first backflow is seen in the ascending aorta. Towards the end of the cardiac cycle the aorta has almost fully returned to its original state.

1.3 Circulation Model

A model of the circulation flow is necessary for the flow simulation in the heart. This should formulate the boundary conditions at the artery exits and the vein entrances of the heart model. The circulation model of Naujokat and Kiencke (2000) takes into account the flow from the left heart ventricle into the aorta and into the attached arterial system of the body circulation, to the venous system, the right heart ventricle, the lung and back to the left ventricle. The circulatory system is divided into i elastic pipe segments. Within the framework of the electrodynamic analogy, whose basis was described by Guyton et al. (1972), the solution of the Navier-Stokes equation for the elastic pipe flow in each segment of the circulation model is found by associating the electric resistance, inductivity and capacity with the physical properties of the arterial and venous branching and the rheological properties of the blood.

The flow velocity v and the pressure p correspond to the electrical current



Fig. 6. Secondary flow in the aorta

strength and voltage respectively. In analogy to the solution of the Navier-Stokes equations, for each elastic pipe segment we have the following ordinary differential equations:

$$p_{i-1} - p_i = \frac{9 \cdot \rho \cdot L}{4\pi^2} \cdot \frac{dv_i}{dt} + \frac{8 \cdot \mu_{\text{eff}} \cdot L}{\pi r^4} \cdot v_i \quad (1)$$

$$= I \cdot \frac{dv_i}{dt} + R \cdot v_i \quad ,$$

$$v_i - v_{i+1} = \frac{3 \cdot \pi \cdot r^3 \cdot L}{2 \cdot E \cdot d} \cdot \frac{dp_i}{dt} = C \cdot \frac{dp_i}{dt} \quad , \quad (2)$$

with the electric resistance R , the inductivity I and the capacity C . L is the pipe length, r the pipe radius, d the wall thickness of the pipe segment, ρ is the density of the blood and μ_{eff} is the blood viscosity. E is Young's elastic modulus of the pipe segment.

Figure 7 shows the 128 branching and pipe segments of the arterial circulation model. The modelling of the vein and lung circulation is carried out analogously, however with a lesser degree of detail. For the flow simulations in section 3 the simplified circulation model of Reik et al. (2005) has been used, which is shown in Figure 7 as well. 7 arterial and 4 venous elastic pipe segments have been used for the flow simulation of the healthy ventricle. For the unhealthy ventricle with aneurysm and the ventricle after surgery no circulation data are available. Therefore, the inflow and outflow pressure have to be set constant.

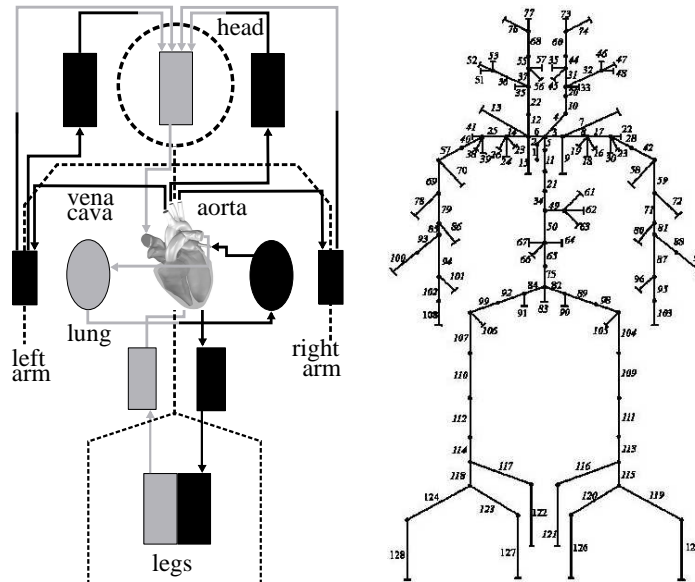


Fig. 7. Circulation model

1.4 Blood Rheology

The *blood* is a suspension consisting of *blood plasma* and 40 to 50 percent of volume of deformable *blood corpuscles*. The red blood corpuscles are deformable disk-like bodies with a length of 8 micrometers. Whereas the blood plasma consists of 90% water and therefore has Newtonian properties, the blood suspension has non-Newtonian properties. To first approximation, the viscous properties of the blood can be described with an effective viscosity μ_{eff} . This increases with decreasing shear rate, due to the increasing accumulation of red blood corpuscles.

Figure 8 shows the dependence of the viscosity μ_{eff} of the blood on the shear rate $\dot{\gamma} = \nabla \mathbf{v}$. In the ventricle, the dominant component of the shear rate tensor has to be chosen for $\dot{\gamma}$. Over a wide range of varying velocity gradients, a drop in the viscosity of up to two orders of magnitude is noted. The region of velocity gradient in a healthy ventricle is in the asymptotic region where the viscosity is almost constant. For ventricle defects at very high velocity gradients and therefore very large shear stresses, there is a deformation of the erythrocytes, which itself affects the viscosity of the blood suspension. At shear stresses over 50 N/m^2 , the erythrocytes begin to pull apart in a spindle-like manner. At shear rates of less than 1, such as those which occur in the back-flow regions of an unhealthy ventricle, aggregation of the erythrocytes occurs. The cells pile up onto one another and form connected cell stacks which are linked together. However, in a healthy ventricle no aggregation takes place. This is because the aggregation time is about 10 s while the pulse is a factor 10 shorter.

The dependence of the shear stress of the blood τ on the shear rate $\dot{\gamma}$ can be described to good approximation with the Casson equation

$$\sqrt{\tau} = \sqrt{\mu_{\text{eff}} \cdot \dot{\gamma}} = K \cdot \sqrt{\dot{\gamma}} + \sqrt{C} \quad . \quad (3)$$

Here K is the Casson viscosity and C the deformation stress of the blood.

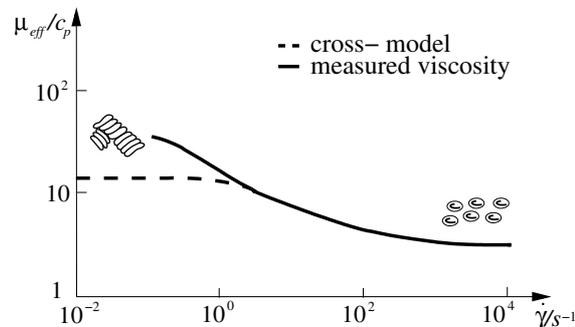


Fig. 8. Blood viscosity

Fitting this equation to experimental results leads to the equation

$$\sqrt{\frac{\tau}{\mu_p}} = 1.53 \cdot \sqrt{\dot{\gamma}} + 2 \quad . \quad (4)$$

with the plasma viscosity $\mu_p = 0.012$ p. For shear rates larger than 100 the blood behaves as a Newtonian medium.

For the numerical calculation of the pulsing blood flow, the modified Cross model of Perktold et al. (1991) is used:

$$\mu_{\text{eff}} = \mu_{\infty} + \frac{\mu_0 - \mu_{\infty}}{(1 + (t_0 \cdot \dot{\gamma})^b)^a} \quad . \quad (5)$$

The constants $\mu_{\infty} = 0.03$ p, $\mu_0 = 0.1315$ p, $t_0 = 0.55$ s, $a = 0.3$ and $b = 1.7$ are adapted to the experiments of Liepsch et al. (1992). Here μ_{∞} is the limiting viscosity for large shear rates $\dot{\gamma}$ and μ_0 is the limiting viscosity for small shear rates.

1.5 Virtual KAHMO Heart Model

The flow simulation in the left human ventricle, atrium and aorta are carried out using the virtual KAHMO heart model (**K**arlsruhe **H**eart **M**odel). The heart model is divided into the active part consisting of the ventricles and the atria; and the passive part with the aorta, vena cava and cardiac valves. The human circulation is taken into account with a circulation resistance and pressure boundary conditions of section 1.3 at the atria, aorta and vena cava

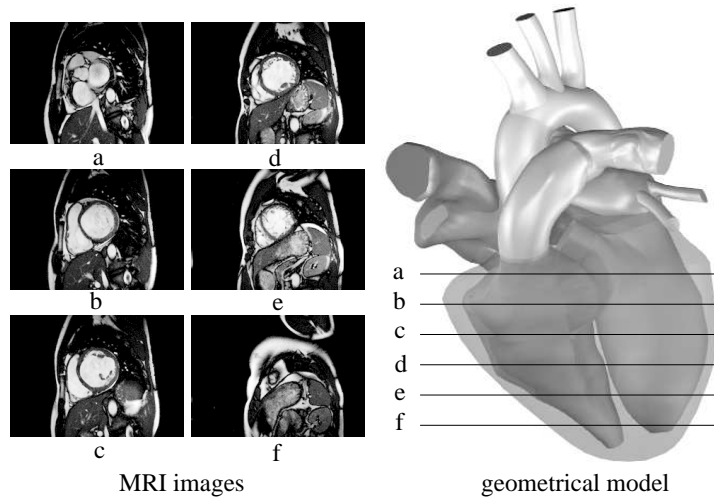


Fig. 9. KAHMO heart model

which have been adapted to MRI-flux measurements.

As there are no in vivo structure data of the human ventricle myocardium available, the model does without an active fluid-structure calculation in the ventricle and replaces these with in vivo measurements of the motion of the human ventricle with image data from nuclear spin MRI tomography. Figure 9 shows horizontal sections of the MRI tomograph of a healthy human heart at a given point in time and the geometry model derived from it. The periodical geometrical model of the human heart is represented at each point in time by 23 horizontal and vertical sections. A cardiac cycle consists of 17 to 25 time steps with a respective time resolution of 32 ms to 45 ms of the MRI tomograph. The geometry data of the periodic ventricle motion is recorded over several cardiac cycles and converted into a CAD geometry model. The trigger for recording the image takes place via the ECG shown in Figure 3.

The passive part of the KAHMO heart model consists of a model aorta, vena cava and pulmonary artery, as well as the heart valve modeling. In the inactive part of the heart, in contrast to the ventricles, the movement is caused by the flow. To calculate the pulsing deviation of the aorta and the cardiac valve motion, a flow-structure coupling is therefore necessary. Since no in vivo stress strain data of the moving walls are available, the moving geometry has been also prescribed by the MRI data, or, if human data are not available, added by generic models.

Supplementary image data and velocity measurements with ultrasonic Doppler echocardiography have been used, which form the basis to develop a simplified model of the heart valves. Instead of all three-dimensional details of the valve motion, only their projection onto the valve plane is modelled, in such a way that the volume fluxes of the human valves are correctly represented.

Figure 10 shows a typical example of the results of flow simulations from section 3.4 with the KAHMO heart model. The results are for the left ventricle,

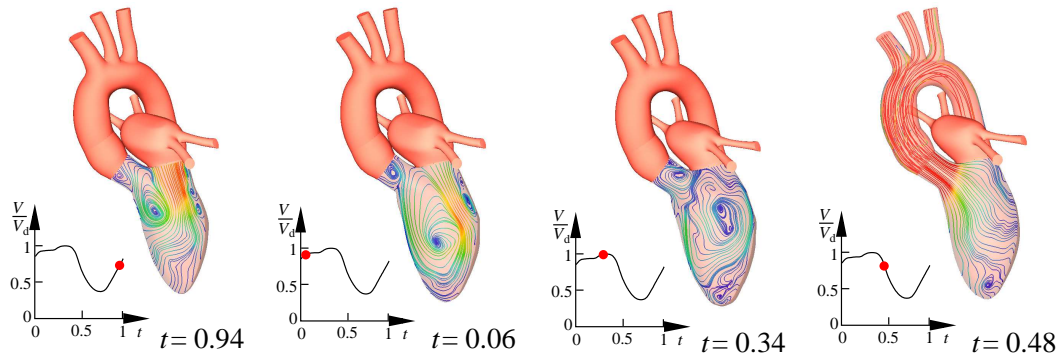


Fig. 10. Flow simulation with the KAHMO heart model, $Re_{D_{\text{systolic}}} = 3700$, $Wo = 24$, $T_0 = 0.76$ s

a generic atrium, and an aorta of a healthy human heart at four points in the cardiac cycle. Each case shows a snapshot of streamlines in the left ventricle projected onto a longitudinal section, as well as the three-dimensional streamlines in the aorta. The intake flow into the left ventricle and the outflow from the atrium as the mitral valve is opened can be seen, along with the intake vortex in the ventricle that accompanies it. This branches according to Figure 4 into two parts, so that the flow also washes through the apex of the ventricle. A clockwise rotating vortex can be observed in the projection plane, as the aortic valve is opened, the first part is initially expelled into the aorta. The streamlines in the aorta branch into each artery and, because of the centrifugal force in the aorta curve, the secondary flow of section 1.2 forms (Oertel (2004), (2005)).

The flow simulation of the healthy human ventricle serves as a reference for the flow simulation of an unhealthy human ventricle with an aneurysm before and after surgery.

2 Ventricle Model

2.1 Geometrical Model

The starting point of the dynamic geometrical model of the moving inner wall of the left ventricle (Fig. 11) is one set of MRI image data of the healthy human heart, a pathological ventricle with aneurysm before and after surgery, taken at the University Hospital of Freiburg (Jung (2003)). The methods of MRI imaging, the segmentation of images and the reconstruction of the geometrical models are described in detail by Schenkel et. al (2007).

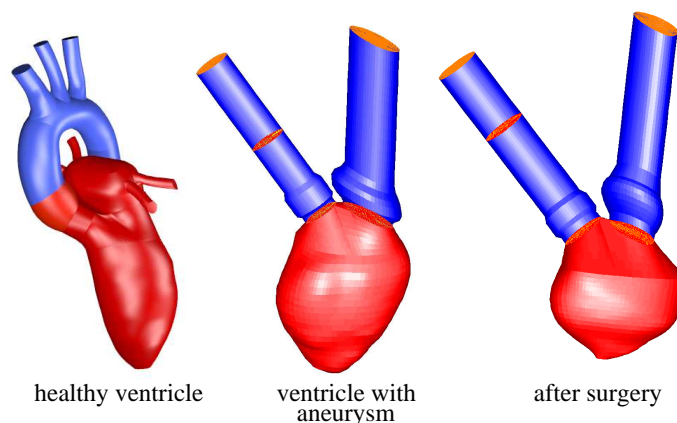


Fig. 11. Geometrical models of a healthy human left ventricle and a human ventricle with aneurysm before and after surgery

MRI Image Data

Eighteen short-axis slices are taken from the top of the heart, through the mitral valve, as well as five vertical sections through the middle of the left ventricle. The sections are rotated about different angles so that the ventricles are seen as fully as possible.

In addition, three sections are taken perpendicular to the aortic valve plane. In fitting the boundary conditions of the calculations and the validations of the results, the blood flow in the heart is determined by means of the MRI phase contrast flow measurements. This must be carried out at the same number of cardiac cycles as the earlier image data. The blood flow is measured perpendicular to the aortic valve and the mitral valve plane, as well as in the so-called three-chamber view of the left ventricle outflow tract.

The problem in producing pictures of the heart is, that the movement of the heart and the fast flow of blood make obtaining meaningful images difficult. The breathing of the patient is a further problem, as the motion of the diaphragm causes displacement of the heart in the chest. Therefore, short exposure times and high resolution are necessary for taking images of the heart. Through employing an electrocardiogram (ECG) and corresponding triggering of the image capture, new MRI data acquisition protocols make it possible to obtain time-resolved cine-records of the heart in a phase of only 15–20 seconds where the breath is held.

The time resolution of the image acquisition is 50 ms and is chosen depending

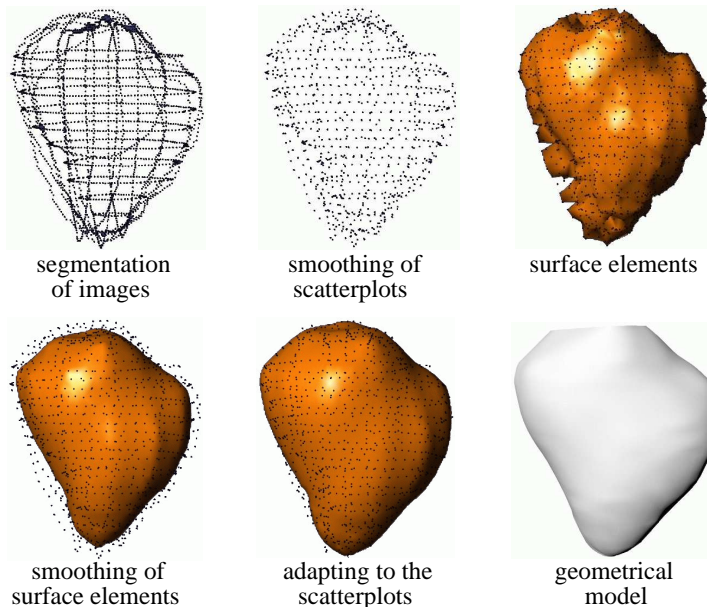


Fig. 12. Reconstruction of the geometrical model

on the frequency of the heart in order to record 17 - 25 time steps of the cardiac cycle. The spatial resolution and thus the thickness of the individual layers is 6 mm.

The demands on the image acquisition and the MRI phase contrast flow measurements, as well as the optimization of the segmentation of the images, are documented in the report by Schwarz (2003) and Oertel (2005).

Segmentation of Images

In order to determine the dynamic geometrical model of the left ventricle, the contours of the left myocardial wall in a cine-heart-MRI image of the human hearts are segmented, in all sections and in all cardiac cycles. The semi-automatic segmentation is carried out using the live-wire method of Mortensen and Barrett (1998). The segmentation method is based on the algorithm of Dijkstra (1959) to optimize the path search in a weighted graph.

Reconstruction of the Geometrical Model

The result of segmentation is a scatter plot of the contour data for each time step. As shown in Figure 12, a smoothing and triangulation tool is used to create a surface that is coincident in geometry and volume with the segmentation data.

2.2 Valve Models

The opening and closing of the mitral and aortic flaps is pressure controlled. Figure 13 shows the systolic opening and closing process of the mitral and aortic valve with an image frequency of 50 Hz. The individual images are taken with a three-dimensional echocardiograph by Handke et al. (2003) and reconstructed three-dimensionally, whereby the systole is covered with 50 images. The flap opening already reaches its maximum early in the systole. After this, closure begins, first taking place slowly and finally quickly. The systolic change of the shape of the opening surface is modelled in the projection onto the valve plane.

Figure 14 shows the resulting two-dimensional model of the mitral and aortic valves. The volume fluxes determined with the MRI phase contrast flow measurements are modelled with opening and closing projection surfaces of variable resistance. The mitral valve has two flaps which are mapped into the

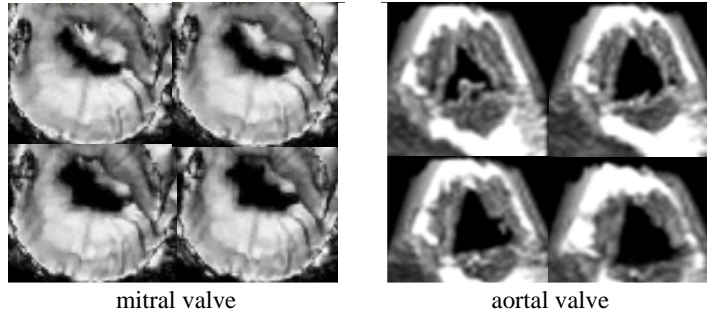


Fig. 13. Opening of the mitral and aortic valve

projection plane with a variable slit diaphragm. The three crescent-shaped connective tissue sacks of the aortic valve are simulated with a pin diaphragm of variable cross-section and resistance.

2.3 Numerical Model

The basis of the numerical model is the geometrical model of Figure 11. The flow in the left ventricle is determined by the motion of the geometrical model. The afterload p_a , forward pressure p_f and the circulation resistance R are taken from a simplified circulation model. The pressure boundary conditions are formulated at sufficient distance from the cardiac valve model in Figure 14 to minimize the influence of the boundary conditions on the flow simulation in the ventricle. The numerical model of Figure 15 is expanded around a generic atrium and a generic aortic root (whose size is adapted to the mitral and aortic valve). For the ventricle with aneurysm and the ventricle after surgery, no in vivo data for the atrium and aorta were available, and so a constant afterload p_a and forward pressure p_f have been assumed.

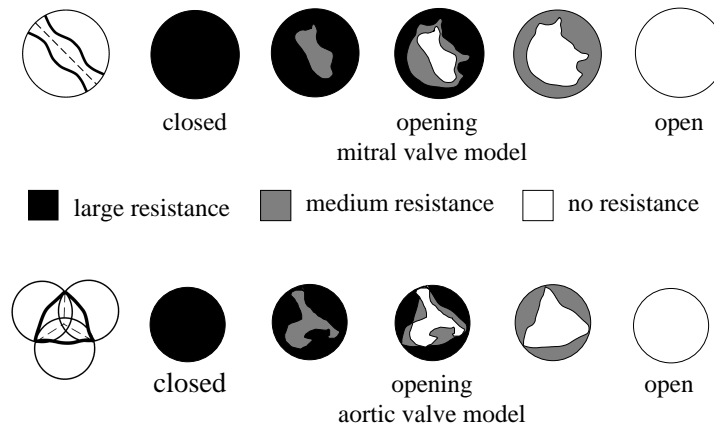


Fig. 14. Mitral and aortic valve model

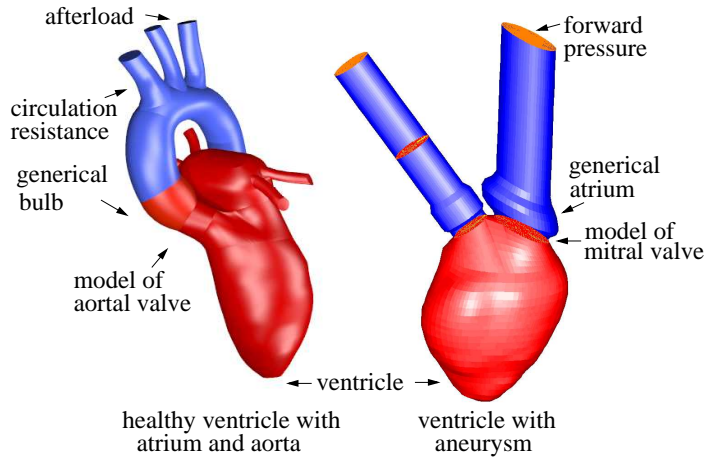


Fig. 15. Numerical models

Computational Grid

The surface of the geometrical model of Figure 12 forms the basis of grid generation. The surface and the fluid space of the ventricle are covered with hexagonal cells, on top of which is placed an O-grid for the ventricle entry and exit. The topology of the computational grid is shown in Figure 16 and 17. At every point in time at which MRI images exist, a separate grid is created. The resulting surface grid is smoothed so that the ventricle volume is kept constant. The grids at each of the 17 time steps are generated so that they are topologically equivalent. The number of nodes and thus of cells is the same in all grids. For the given resolution of 17 grids over the cycle, 50 intermediate steps are needed for the grid used to keep the Courant number Co for the flow simulation close to unity.

The position of the nodes in the grid as well as their identification number also remains constant at each point in time. From the position of the node i at time t_n and at time t_{n+1} , intermediate grids are determined. Nonlinear interpolation is performed between the individual grids, so that it is ensured that the position vectors x_{n-1} and x_{n+1} pass continuously into each other.

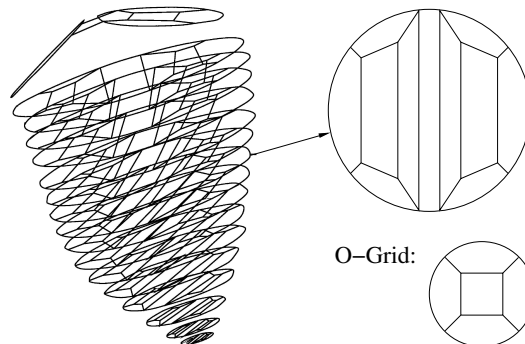


Fig. 16. Topology of the computational grid

The motion of the ventricle is different in different regions. The motion of the cardiac valve plane is small compared to the motion in the apex of the heart. Therefore, some sections of the grid, those that can be recognized clearly in the MRI images, are fixed. The remaining grid planes are distributed linearly between these. The global motion of the ventricle is therefore divided into regions of differently sized motion.

The flow structure in the ventricle to be calculated is dependent on the number of cells in the computational grid (see Oertel (2005), Oertel and Laurien (2003)). Therefore, first the grid dependence of the numerical solution in the ventricle described in the following section has to be analyzed. In Figure 18 the velocity profiles along the sketched ventricle section are plotted for $5 \cdot 10^4$, $1 \cdot 10^5$ and $2 \cdot 10^5$ grid cells at the diastolic time $t = 1$. The velocities near the mitral valve inflow area agree well, as well as with MRI-velocity measurements, while the $5 \cdot 10^4$ grid simulations show discrepancies in the area of the aortic channel.

The global flow structure is within segmentation accuracy independent of the number of cells for a computational grid of more than 10^6 cells for the ventricle calculations and cells for the atrium. With the selected time step size of $\Delta t = 0.89 \cdot 10^{-3}$, we obtain a Courant number of $Co = 6$. This is taken as a basis for the flow simulations in the following sections.

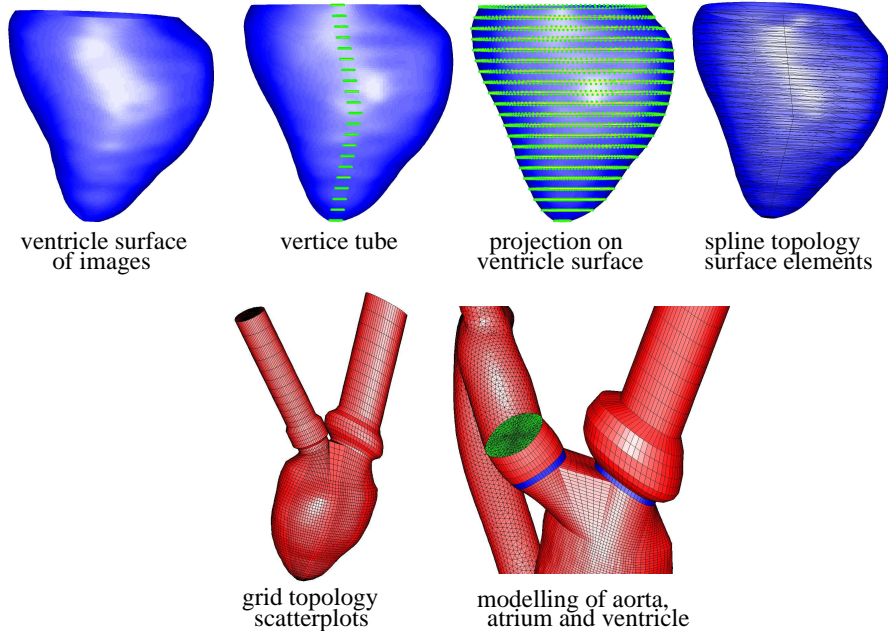


Fig. 17. Computational grid

3 Aorta Model

In order to calculate the model aorta that forms the inactive part of the healthy KAHMO heart model, a flow-structure coupling is necessary. The pulsing blood flow of the left ventricle causes a deviation of the aorta that is accompanied by an increase in volume. Therefore the motion cannot be predicted for the flow calculation, but rather must be determined via a structure calculation. The model aorta is to approximate the natural aorta as closely as possible with respect to its elastic properties. The assumption of a model aorta is justified, as in general no MRI images of the aorta are taken in clinical investigation of the human heart.

The model aorta was generated by discharge of an aorta specimen by Liep-sch et al. (1992). The aorta is that of a young woman without pathological conditions. In order to attain good fine structure accuracy, the discharge was carried out post mortem. Different levels of molding led to a build-up of silicon in the aorta specimen, corresponding to the elastic properties of the human aorta.

3.1 Geometrical Model

The geometrical model of the silicon specimen of the model aorta is shown in Figure 19. It consists of the ascending and descending aorta as well as the exits to the collar bone and neck arteries in the bend in the aorta. The connection to the left ventricle is via a flexible generic aortic root that models the transition upstream of the aortic valve.

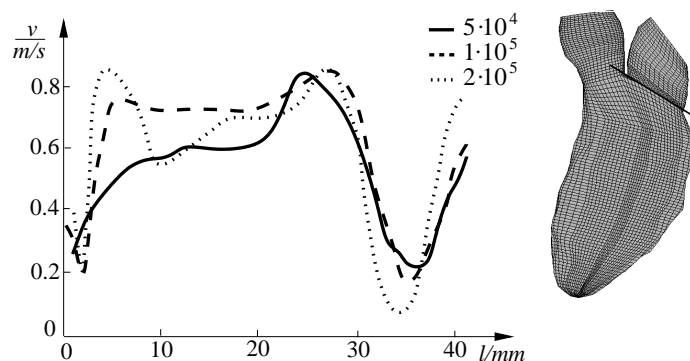


Fig. 18. Computational grid dependence of the ventricle velocity profiles

3.2 Flow-Structure Coupling

To calculate the structure of the aorta, a first linear approach is made using the software package Permas. The software package is based on the finite element method. The spatial discretization is carried out using form functions that are weighted with the functional values in the elementary nodes. The stress-tension properties of the aorta are taken from the literature. The flow-structure coupling is partitioned. The flow and structure fields of the aorta are calculated separately and suitable load quantities such as the pressure and the shear stress components are compared after every time step. The transfer of the shear stress tensor of the flow calculation onto the nodes of the structure program is performed using the coupling library MpCCI. An important condition for successful coupling of the different computational grids of the flow and structure calculation (Fig. 20) is an efficient algorithm to automatically search for neighborhoods in the computational grids. To this end a Bucket algorithm is employed.

The disadvantage of the weakly partitioned coupling of the flow calculation with the linear structure calculation is the fact that no equilibrium position can be calculated. As it is only the calculation of the volume reservoir of the aorta integrated into the circulation model and the flow drag that are of interest within the framework of the KAHMO heart model, the selected coupling model is sufficient. However, if we are interested in the details of the coupling mechanism, a more strongly nonlinear and iterative coupling algorithm must be selected.

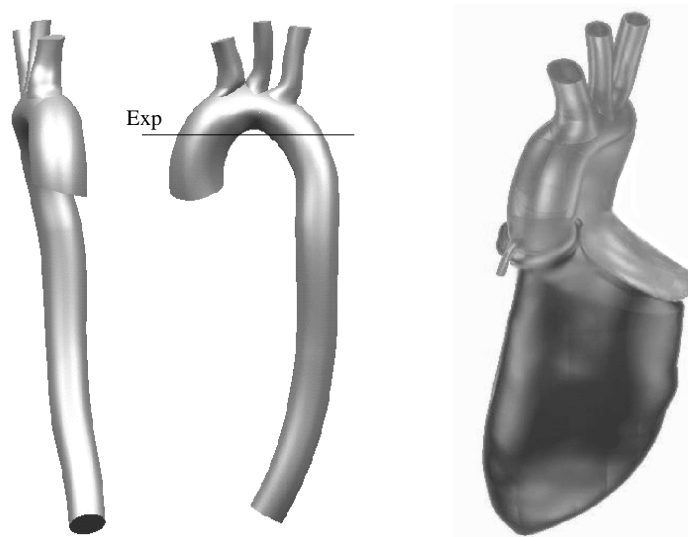


Fig. 19. Geometrical model of the aorta

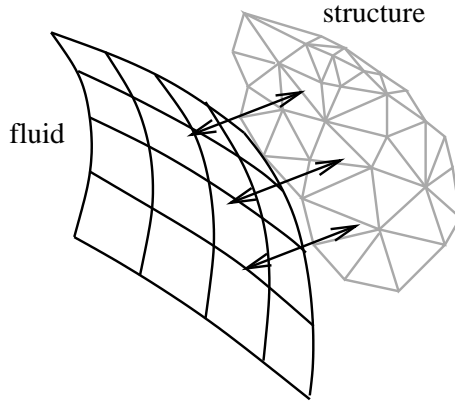


Fig. 20. Exchange of flow and structure quantities with the coupling library MpCCI

3.3 Numerical Model

The numerical model to calculate the flow in the model aorta is shown in Figure 15. At the intake edge of the ascending aorta, the velocity distribution of the ventricle calculation is given. At the exit edge of the branching and descending aorta, each of the pressures and circulation resistances calculated with the circulation model are given. Using the pressure given by the boundary conditions, the stress-free exit geometry of the model aorta is prescribed.

Generation of the computational grids and the demonstration of the grid independence of the simulation results is carried out in the same way as in Section 2.3.

3.4 Validation

Validation of the flow-structure coupling model is carried out using the silicon aorta specimen (Liepsch et al. (1992)). The silicon has isotropic material properties with E-modulus $E = 1.9 \cdot 10^6 \text{ N/m}^2$, transverse contraction number $r = 0.49$, density $\rho_s = 970 \text{ kg/m}^3$ and refractive index $n = 1.413$, corresponding to the transparent model fluid. It is known from expansion measurements that the aorta specimen can be approximated with a linear constitutive relation.

The measurement of the local velocities in selected sections of the model aorta is carried out using laser-Doppler anemometry (LDA). The pulsing flow in the aorta specimen is given by the healthy model ventricle of Section 4.3. The same parameters are chosen for the numerical flow simulation of the elastic aortic bend as in the experiment.

The wall strength distribution of the aortic model is matched to the wall strength of the aortic specimen in experiment (Fig. 21). In the experiment the aortic specimen is attached at its entrances and exits with plexiglas tubes. For the structure-mechanical calculation this means that the freedom of motion at these edges is restricted. Therefore, just as with the structure calculation at the edges, all degrees of freedom are suppressed.

Comparison of the flow calculation with the model aorta and the experiment in the aorta specimen shows good agreement during the systole. Differences between the measurement and the simulation calculation appear at the start of the diastole as the flow slows down in the ascending and descending aorta. In the experiment there is a uniformly small backflow in the ascending aorta. At the same point in time, the velocity in the simulation calculation sinks to a minimum, although it is still positive. This may be due to the different formulation of the circulation and boundary conditions. The deviation and the volume change of the model aorta is correctly given by the simulation results with the simplified linear flow structure coupling, so that the aim of the validation is attained, namely the calculation of the flow losses and pressure boundary conditions of the aorta in the circulation model.

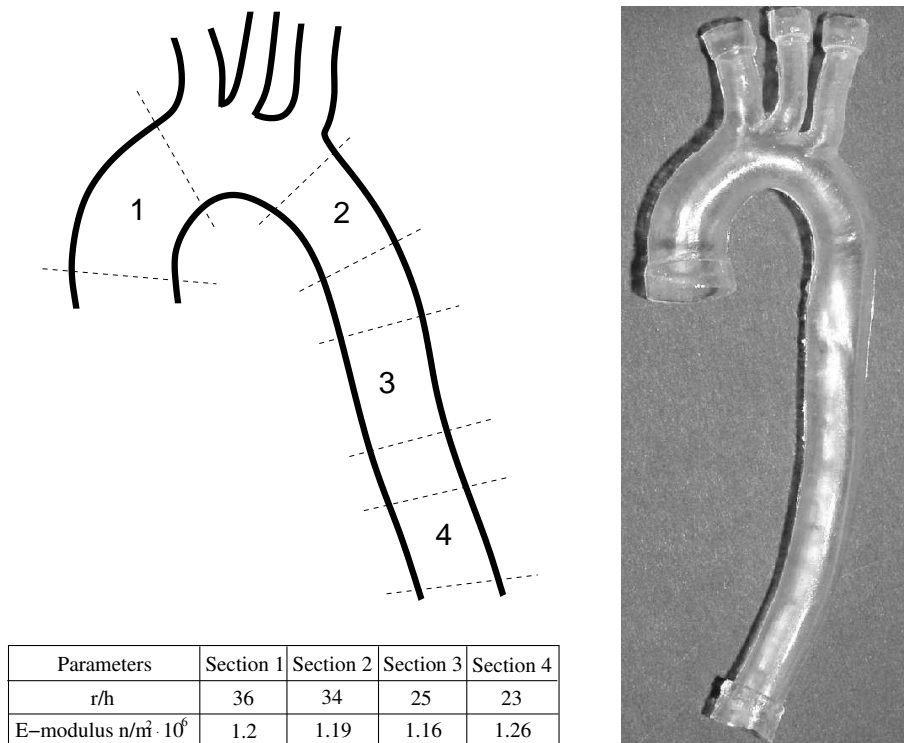


Fig. 21. Segments of the aortic specimen and the wall properties

4 Flow Simulation

4.1 Basic Equations

For the calculation of the incompressible pulsating flow in the human left ventricle, the continuity and Navier-Stokes equations are made dimensionless with the characteristic diameter of the aorta D and the mean velocity U :

$$x^* = \frac{x}{D} \quad , \quad v^* = \frac{\mathbf{v}}{U} \quad , \quad t^* = t \cdot \omega \quad , \quad p^* = \frac{p}{\rho \cdot U^2} \quad .$$

Using the dimensionless characteristic Reynolds number $Re_D = U \cdot D / \nu_{\text{eff}}$, with $\nu_{\text{eff}} = \mu_{\text{eff}} / \rho$ from equation (3) and Womersley number $Wo = D \cdot \sqrt{\omega} / \nu_{\text{eff}}$ ($\omega = 2 \cdot \pi / f$), we obtain the dimensionless equations:

$$\nabla \cdot \mathbf{v} = 0 \quad , \quad (6)$$

$$\frac{Wo^2}{Re_D} \cdot \left(\frac{\partial \mathbf{v}}{\partial t} + (\mathbf{v} \cdot \nabla) \mathbf{v} \right) = -\nabla p + \frac{1}{Re_D} \cdot \Delta \mathbf{v} \quad . \quad (7)$$

The force tensor which acts on the flow from the inner walls of the heart is replaced by the movement of the geometrical model.

4.2 Numerical Algorithms

The numerical solution of equations (6) and (7) is carried out using the finite volume method and the numerical model of the previous section. The flow calculation is performed using the Star CD software package (Computational Dynamics Limited (2003)). It has been verified for numerous applications in fluid mechanics, especially for rigid and elastic pulsative pipeflows, Oertel et al. (2006), Oertel and Laurien (2003). The time discretization is performed with an implicit Euler method and the monotonic advection and reconstruction scheme. This second-order method is carried out in two steps. First of all, a field of monotonic gradients is defined, that together with the finite volume discretization guarantees a spatial second-order discretization. In the second step the fluxes through the volume cell surface for all advectively transported quantities are reconstructed from the quantities calculated in the first step by means of a monotonic and bounded advection scheme. In order to calculate the incompressible blood flow, the PISO algorithm is applied. This introduces a further equation to calculate the pressure field. The PISO algorithm

is a predictor-corrector method that calculates the temporally implicitly discretized unsteady flow. The details of the temporal and spatial discretization may be found in Oertel and Laurien (2003).

4.3 Model validation

The validation of the KAHMO ventricle model was carried out by Liepsch et al. Liepsch et al. (1992) and Schmid et. al (2005). In the experiment, the artificial ventricle consists of a special silicon mixture with elastic properties, adapted to those of the myocardium, and is made to undergo the cyclical ventricle motion in a pressure chamber. The periodic flow into and out of the ventricle is controlled by two artificial biological three-flap heart valves that are connected to tubes that generate the preload and afterload as well as the circulation resistance.

The transparent liquid in the ventricle and in the pressure chamber is a glycerine-water mixture with the viscosity of blood. Velocity measurements in the long axis planes of the ventricle are performed using particle image velocimetry (PIV).

The KAHMO geometry model is adapted to the experimental motion of the ventricle at 18 points in time. The matching of the mitral and aortic valve models is carried out by measuring the flow rate through the artificial heart valves. Figure 22 shows the comparison between the measured and calculated velocities at two times of diastole and systole. There are variations between the experiment and simulation in the intake jet, but the maximum velocity

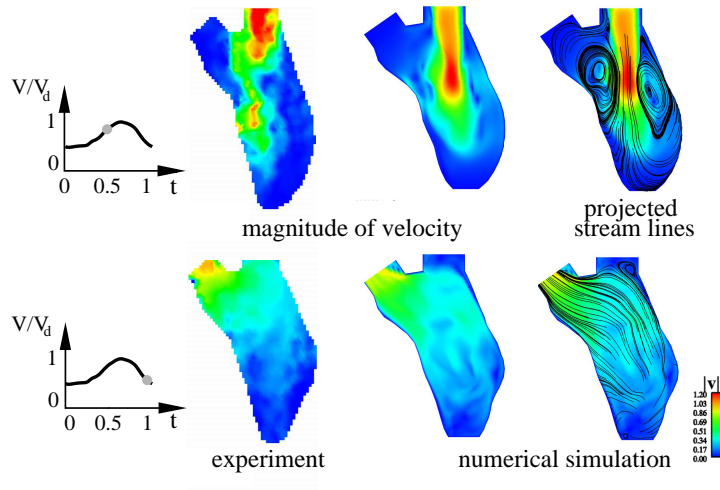


Fig. 22. Model validation of left ventricular flow, Experiments Liepsch et al. (1992), Schmid et. al (2005), $Re_{D,\text{systolic}} = 3700$, $Wo_{\text{systolic}} = 28$

of 3.7 m/s is the same in both. Both, the experimental velocity profiles and the streamlines calculated and projected onto the long axis plane, indicate asymmetric deformation of the intake vortex, with branching into the apex of the ventricle as well as the exit flow process during systole. Thus, the validation experiment satisfies all criteria of the pulsing flow in the human heart as described in Section 1.

4.4 Model predictions

Ventricle flow

The flow calculations are carried out for three sets of data of the human heart. F001 is the set of reference data for the healthy heart. F002-pre is the set of data for a heart suffering from aneurysm before the ventricle operation, while F002-post is that after the ventricle surgery.

Table 1 summarizes the anatomical and physiological parameters of the ventricle simulations. Figure 23 shows the results of simulation. Streamlines, streamlines projected along the long axis plane and the magnitude of the velocity vector are shown in color. Red means high velocities. In the healthy heart, the pulsing flow described in Section 1.1 is observed. At the time $t = 0.76$ the mitral valve opens. At $t = 0.94$ the intake flow process in the ventricle is fully developed. At $t = 0.06$ the intake vortex forms in the empty part of the ventricle. This expands asymmetrically and branches up to $t = 0.29$. At $t = 0.34$ the intake flow process is complete, and the flow vortex is orientated to prepare for the exit flow through the aortic valve. At $t = 0.37$ the aortic valve opens and the expulsion into the aorta begins. At $t = 0.48$ the exit flow process is fully developed.

Shortly after the mitral valve opens, the streamlines in the upper part of the ventricle are arranged almost parallel and are directed towards the apex of the ventricle. The fluid in the lower part of the ventricle has not yet been reached by the movement of the intake flows. The intake process gives the streamlines their orientation in the whole ventricle. The fluid passes through the entire surface of the mitral valve with its maximum velocity. The blood flowing into the ventricle is slowed down by the blood at rest in the ventricle, and a ring vortex with foci (F1) and (F2) is formed in the upper part of the ventricle. The ring vortex has the shape of a torus and the fluid passes the surface of this torus along the shortest path. The direction of motion of the fluid can easily be seen in the long axis plane.

The reason for the formation of a ring vortex is, that the velocity of the incoming blood in the upper part of the ventricle is larger than that in the lower part. The blood at rest in the ventricle is accelerated by the intake jet, but is

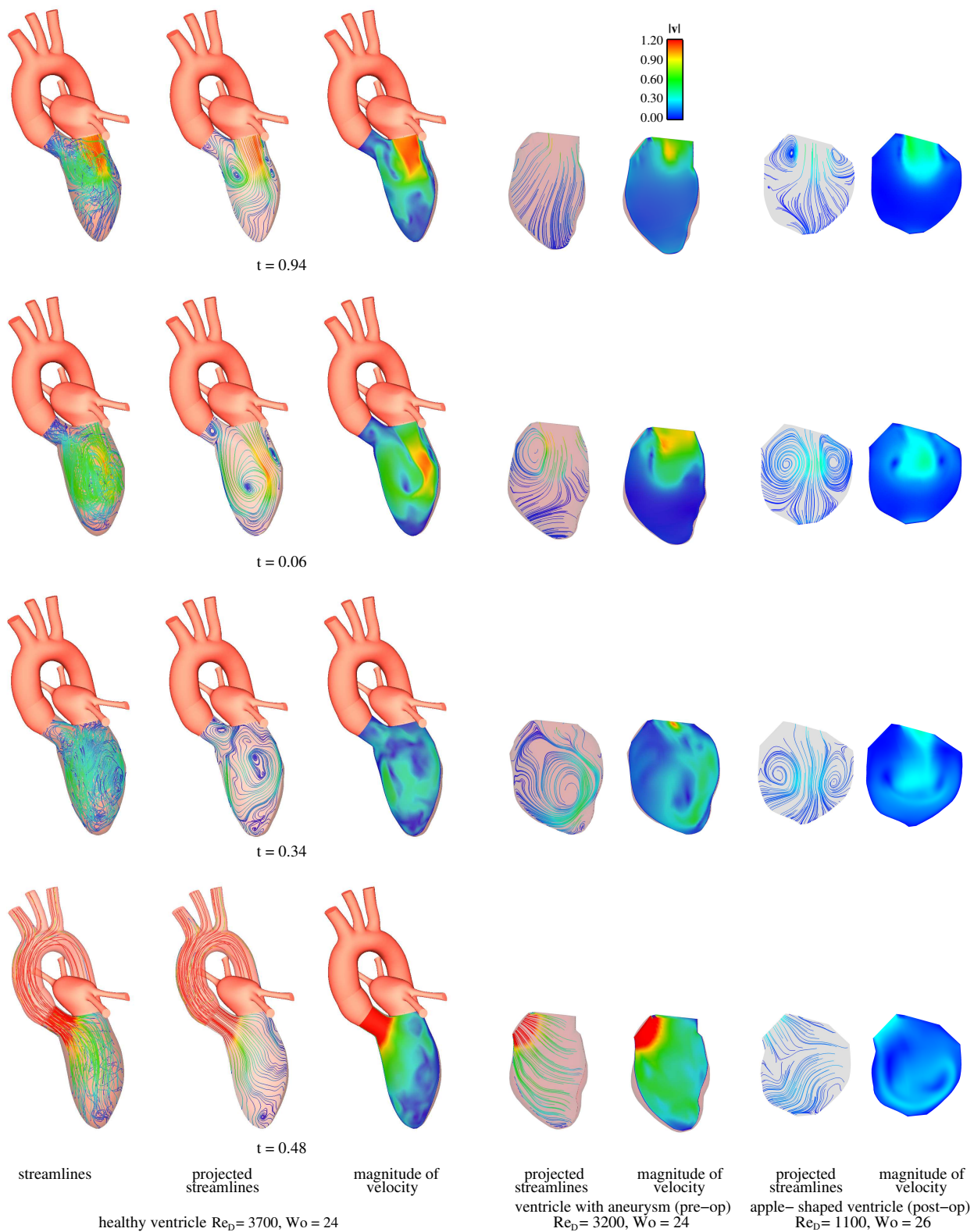


Fig. 23. Numerical results of the ventricular flow

unable to pass into the lower part of the ventricle. The ring vortex arises to balance this motion. As diastole continues, the ring vortex increases in size. Its expansion in the axial direction is uniform, however the expansion in the radial direction is considerably greater on the left-hand side than on the right. As a consequence an asymmetrical three-dimensional ring vortex forms with a clockwise rotating focus in the long axis plane, which is in agreement for example with Nakamura et. al (2003) or Long et al. (2003). The cause of this is the motion of the ventricle. During diastole, the ventricle stretches more to the right than to the left, where it is connected to the right ventricle. Throughout the rest of diastole, a further expansion of the ring vortex on the right-hand side can be seen, until finally there is only a small change in volume of the ventricle. The intake process is then complete. The deformation of the vortex structure at this point in time is determined by the inertia of the vortex. The left part of the ring vortex moves towards the middle of the ventricle. Finally,

Parameters	F001 healthy	F002 pre	F002 post
stroke volume V_s :	$9.07 \cdot 10^{-5} \text{ m}^3$	$1.38 \cdot 10^{-4} \text{ m}^3$	$5.46 \cdot 10^{-5} \text{ m}^3$
end diastolic volume V_d :	$1.43 \cdot 10^{-4} \text{ m}^3$	$3.68 \cdot 10^{-4} \text{ m}^3$	$2.31 \cdot 10^{-4} \text{ m}^3$
end systolic volume V_{sys} :	$5.28 \cdot 10^{-5} \text{ m}^3$	$2.31 \cdot 10^{-4} \text{ m}^3$	$1.76 \cdot 10^{-4} \text{ m}^3$
total cycle time T_0 :	0.76 s	0.94 s	0.81 s
systolic time t_s :	0.29 s	0.35 s	0.34 s
diastolic time t_d :	0.47 s	0.59 s	0.47 s
mitral valve surface A_M :	$4.43 \cdot 10^{-4} \text{ m}^2$	$1.01 \cdot 10^{-3} \text{ m}^2$	$7.89 \cdot 10^{-4} \text{ m}^2$
aortic valve surface A_A :	$3.08 \cdot 10^{-4} \text{ m}^2$	$4.43 \cdot 10^{-4} \text{ m}^2$	$5.03 \cdot 10^{-4} \text{ m}^2$
aortic valve diameter D_A :	$1.98 \cdot 10^{-2} \text{ m}$	$2.38 \cdot 10^{-2} \text{ m}$	$2.53 \cdot 10^{-2} \text{ m}$
mitral valve diameter D_M :	$2.37 \cdot 10^{-2} \text{ m}$	$3.58 \cdot 10^{-2} \text{ m}$	$3.17 \cdot 10^{-2} \text{ m}$
forward pressure P_f :	940 Pa	500 Pa	500 Pa
resistance coeff. valves:	5	5	5
porosity P valves:	0.5	0.5	0.5
mean velocity (diastole) v_{dia} :	$4.39 \cdot 10^{-1} \frac{\text{m}}{\text{s}}$	$2.33 \cdot 10^{-1} \frac{\text{m}}{\text{s}}$	$1.48 \cdot 10^{-1} \frac{\text{m}}{\text{s}}$
mean velocity (systole) v_{sys} :	$1.00 \cdot 10^0 \frac{\text{m}}{\text{s}}$	$8.83 \cdot 10^{-1} \frac{\text{m}}{\text{s}}$	$3.17 \cdot 10^{-1} \frac{\text{m}}{\text{s}}$
mean viscosity $\overline{\mu_{\text{eff}}}$:	$5.56 \cdot 10^{-3} \frac{\text{kg}}{\text{ms}}$	$6.59 \cdot 10^{-3} \frac{\text{kg}}{\text{ms}}$	$7.67 \cdot 10^{-3} \frac{\text{kg}}{\text{ms}}$
density ρ :	1008 kg/m ³	1008 kg/m ³	1008 kg/m ³
Re_D (systolic):	3700	3200	1100
Wo (systolic):	24	24	26

Table 1. Anatomical and physiological parameters of ventricle simulations

a three-dimensional branching of the asymmetrical ring vortex takes place and a new focus (F3) and a saddle point (S) in the long axis plane are formed, as shown in Figure 24. The focus (F1) moves off in the direction of the aortic valve.

At the beginning of the systole, the fluid begins to pass out of the ventricle in a well ordered time sequence as the aortic valve begins its opening phase. The bifurcated ring vortex thus keeps moving in the same direction. The focus (F1) of the right part of the vortex is already washed out at the time $t = 0.40$ and it pulls the left focus (F2) after it. The focus (F3) within the ventricle apex has increased in size. The velocity maximum of the exit flow process is reached in the central region of the aortic valve surface and a jet flow forms in the aorta. At $t = 0.48$ the exit flow is fully developed.

The vortex structure is still partially in place and will completely dissipate at the end of systole. The blood now flows through the entire aortic valve surface with its maximum velocity. A ventricle with an aneurysm has the same topological flow structure during diastole as the healthy ventricle. However, because the aneurysm causes the left lower side of the ventricle to sag outwards, the intake vortex is asymmetrically deformed and branches in the middle of the ventricle immediately after it forms, leading to large flow losses during diastole. As the diastole continues, the focus (F1) and hence the saddle point (S) move towards the ventricle wall. Because the branching occurs too early, two further foci (F4) and (F5) form temporarily in the long axis plane at the upper edge of the mitral valve. During the closing phase of the mitral valve, the intensity of focus (F2) increases, related to a smaller vortex in the outwardly sagging region close to the apex of the heart. The outflow process during systole is the same as that of the healthy heart. First focus (F2) and then focus (F3) travel out from the apex of the heart, and more blood remains in the ventricle with aneurysm than in the healthy ventricle.

The flow portrait of the heart that has undergone surgery is completely different. The outward sagging due to the aneurysm has been removed in the operation and a so-called "apple-shaped" ventricle has been created. This means, that during diastole the intake jet is no longer slowed down by the blood at rest up to the apex of the ventricle. Hence, a stagnation point flow arises. The branching is no longer asymmetrical as in the unhealthy heart before surgery, but rather a further ring vortex appears temporarily in the lower region of the "apple-shaped" ventricle. This disturbs the exit flow process during the systole. First the focus (F1) passes through, while the counter-rotating focus (F2) remains in the ventricle and weakens as the systole continues. More blood remains in the post-surgery ventricle than in the ventricle before surgery. At the same time, the shear rates and thus the friction losses between the counter-rotating foci (F1) and (F2) have increased.

Aorta flow

With the validated flow-structure coupling of the aorta model of Figure 17 simulation calculations are carried out. In contrast to the aortic specimen of the validation experiment of section 3.4, now the stress-tension model and the wall strength distributions of the human aorta are used.

Figure 24 shows the calculated three-dimensional streamlines and the velocity profiles during one cycle. At the beginning of the systole the flow in the model aorta quickly reaches its maximum and already exhibits a considerable deformation at $t = 0.43$. As expected from Figure 6, the flow profiles have a maximum at the inner side of the aortic bend. After passing through the entire curved region, the maximum shifts to the outer side of the aortic bend. The streamlines at the time $t = 0.43$ already indicate the secondary flow in the aortic bend. At time $t = 0.63$, the point of maximum deceleration of the flow occurs. The velocity profiles flatten and the streamlines indicate a first backflow in the ascending branch of the aorta. At time $t = 0.85$, the aorta has almost completely returned to its initial position.

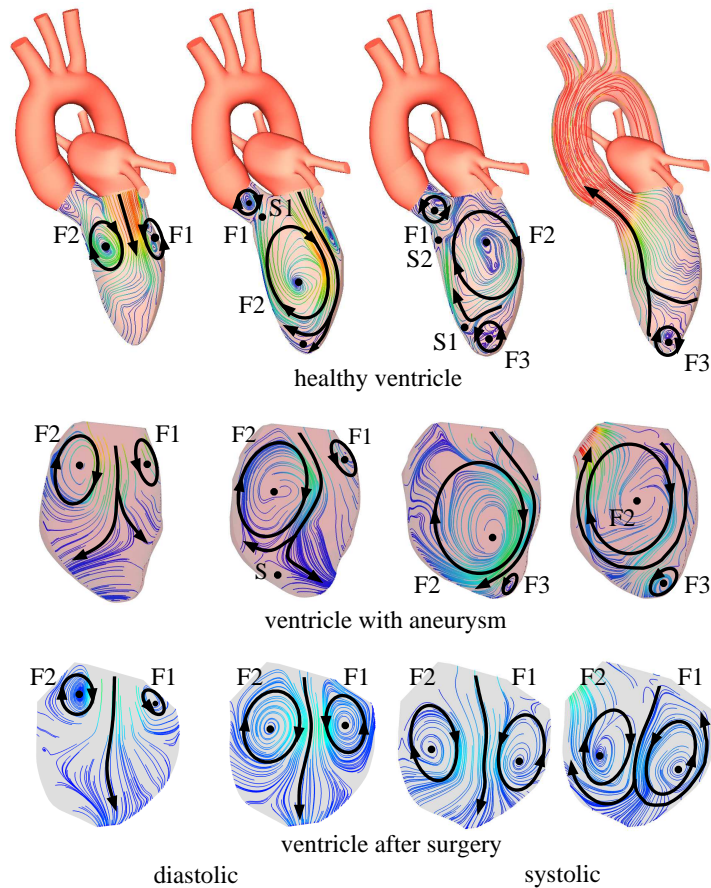


Fig. 24. Flow structures of healthy ventricle, ventricle with aneurysm and ventricle after surgery

In the ascending model aorta, a strong deviation due to the pressure pulse is observed. It is to be noted that the bulging deformation of the aorta in this region is caused by the close structure boundary condition at the aortic root. During the systole, because of the centrifugal force, the secondary flow forms two vortices with two half-saddles. This structure is retained into the diastole. In spite of the deceleration of the flow that has already begun, the compliance of the aorta clearly contributes to a stabilization of the flow structure. At time $t = 0.85$ the structure finally breaks up. The main flow velocities are close to zero and the deformation of the aorta is again the same as its initial condition.

At the start of the systole there is still no evident secondary flow, and it is only at $t = 0.43$ that the first structures of the secondary flow can be seen. At time $t = 0.63$ the radial deviation motion of the aorta as already described can be observed. For a short time a triple-vortex configuration appears, only to decay again to the stable double vortex at $t = 0.67$. This double vortex structure of Figure 6 remains for the rest of the cardiac cycle.

5 Discussion and Model Conclusions

The first parameter used to characterize the fluid mechanics of ventricular flow is the ejection fraction of the ventricle

$$E = \frac{V_s}{V_d} \quad . \quad (8)$$

with the stroke volume V_s and the end diastolic volume V_d . As shown in Table 2, the ejection fraction of the healthy human heart is $E = 63\%$. The ventricle with an aneurysm has an ejection fraction of 37% , while the value for the "apple-shaped" post-surgery ventricle is only 24% . Therefore, the values of the ejection fraction also indicate that the stagnation point flow is an ineffective flow through the ventricle with regards to flow losses.

Figure 25 shows the change in volume through one cardiac cycle of the healthy ventricle and of the diseased ventricle before and after surgery. The dimensionless volumes are each related to the corresponding volume V_d at the end of the diastole. In Figure 26 the p-V-diagram for the healthy ventricle is plotted including the segmentation error bars. The dashed line indicates the averaged p-V profile.

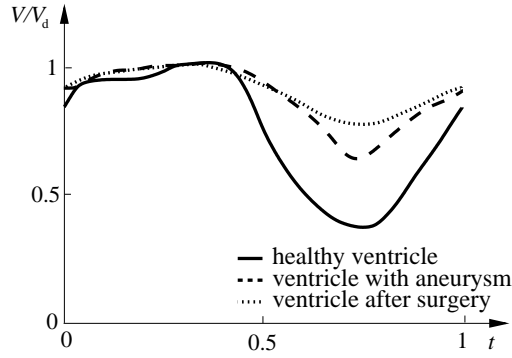


Fig. 25. Ventricles volumes

Another way of characterizing the flow in the ventricle is by means of the mixing parameter M of the blood in the ventricle.

$$M = (1 - E)^n \quad . \quad (9)$$

E is the ejection fraction (8) and n is the number of cardiac cycles that must pass until the blood in the ventricle is fully exchanged. In the simulations, a scalar is initialized at the mitral valve to represent the mixing of the old blood in the ventricle with the new blood flowing in.

Figure 27 shows, that in the healthy ventricle with ejection fraction $E = 0.63$, after one cardiac cycle $M = 0.37$ of blood remains in the ventricle. After the second cycle, 16% of the original blood remains, while after three cardiac cycles 7% remains. Thus, in the healthy ventricle, the blood is exchanged within three cardiac cycles. The values of the mixing parameter are correspondingly higher for the ventricle with an aneurysm and the post-surgery ventricle. Because of the unsteady intermixing of old and new blood during the cycle, the simulations show variations from the theoretical result that assumes a 100% intermixing. However, to compare the three cases M can be considered as a helpful parameter for medical decisions.

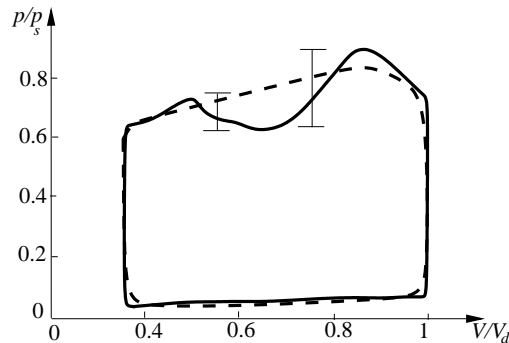


Fig. 26. p-V diagram

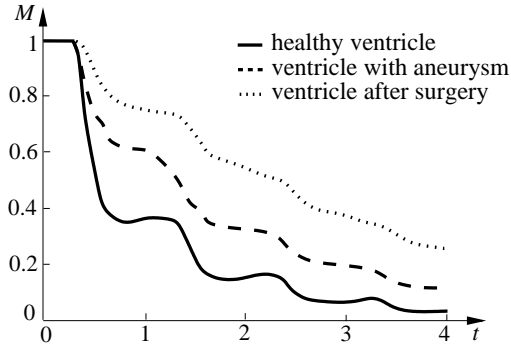


Fig. 27. Mixing parameter

A further way of evaluating the reconstruction of the ventricle before and after surgery is the ventricle work performed. This can be derived from the p-V diagram in Figure 26. The relationship between the work done in pumping A_p , the time the blood remains in the ventricle t_b , the mean effective viscosity μ_{eff} (5) and the stroke volume V_s leads to the definition of a dimensionless pumping parameter O , that describes a dimensionless ratio of volumes:

$$O = \frac{A_p \cdot t_b}{\mu_{\text{eff}} \cdot V_s} . \quad (10)$$

The dimension analysis (Oertel et al. (2006)) leads to

$$O = f(Re_D, Wo) . \quad (11)$$

The value $5.8 \cdot 10^6$ of the healthy ventricle has been determined from the p-V diagram of Figure 26. Further ventricle flow simulations for several ventricle reconstruction have to be done to determine the function f for evaluating surgery reconstructions.

Because of the alteration in the flow cycle described in the previous section, the work done in pumping is less in the ventricle with aneurysm and the post-surgery ventricle than in the healthy ventricle. The time the blood remains in

Parameters	F1 healthy	F1 pre	F1 post
E:	63%	37%	24%
M (1. cycle):	37%	61%	74%
M (2. cycle):	16%	33%	55%
M (3. cycle):	7%	20%	38%
O:	$5.8 \cdot 10^6$	—	—

Table 2. Parameters to characterize the fluid mechanics of ventricle flow

the ventricle increases while the stroke volume decreases, so that the surgery parameter then increases.

However, after a successful surgery, the dimensionless parameter ought to decrease to the value for a healthy heart. This indicates to the surgeon that an "apple-shaped" ventricle reconstruction is fluid mechanically ineffective with the stagnation point flow shown. The so-called "cone-shaped" ventricle reconstructions of Figure 28 are preferable, as these demonstrate flow branching into the apex of the ventricle as discussed in the previous section. The flow losses are reduced and the blood is ejected properly during systole.

Whereas the changes in volume shown in Figure 25 are continuous, the lack of more detailed patient specific MRI images and the limits of the pressure boundary conditions in the KAHMO cardiac model are noticeable in the changes in pressure seen in the p-V diagram for flow simulations of the ventricle with aneurysm and the post-surgery ventricle. Because of the low load that can be placed on patients, only MRI images of the ventricle are available. Matching the aorta and atria as in the geometrical model in Figure 10 is not possible. For this reason, instead of employing the pressure boundary conditions determined with the circulation model at the atrium and at the exits from the aorta, constant pressures are assumed at the mitral valve entrance and at the aortic valve exit. These pathologically incorrect pressure boundary conditions mean that the isovolumetric ventricle contraction is not correctly reproduced, but the flow structure in the ventricle as described in the previous section remains unchanged. The flow simulations can be improved by getting more detailed patient specific MRI images.

As in Section 2.1, MRI images are taken at 17 points in time of the cardiac cycle. This means that the computational grid of the ventricle has to be inter-

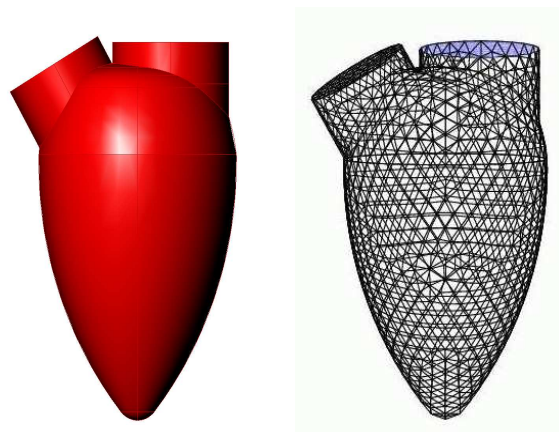


Fig. 28. cone-shaped ventricular reconstruction

polated from one point in time to the next. Until now quadratic interpolation has been used in the KAHMO heart model. This means that the discontinuity in the higher derivatives leads to discontinuities in the pressure. Higher order interpolation of the geometrical model and computational grids is envisaged for the further development of the KAHMO heart model.

Now that in vivo motion data of the myocardium have become available with the MRI phase-mapping method, the next step in the development of the KAHMO heart model is to take into account the flow-structure coupling. This will improve the modelling of the contraction and relaxation phases in the ventricle. Concerning the dimension analysis (12) an additional myocardium parameter has to be added:

$$O_{fsi} = f_{fsi}(Re_D, W_o, E) \quad . \quad (12)$$

E describes the integral nondimensionalless Energy function of the myocard, the derivation of which is subject of further research- and flow-structure coupled simulations.

This second edition of the article shows, that even the current state of development of the KAHMO heart model gives heart surgeons an important indication of how a successful ventricle reduction can be carried out. A cone-shaped ventricle most closely matches the flow branching in the diastole, and so is fluid mechanically the better solution.

Acknowledgements

This work was made possible by the enthusiastic collaboration of T. Schenkel, M. Malvè, M. Reik and S. Krittian of the Institute for Fluid Mechanics at the University of Karlsruhe. We appreciate the support of B. Jung for taking the MRI images at the University Hospitals of Freiburg, as well as R. Schwarz for converting the images at the Fraunhofer Institute for Applied Information Technology. D. Liepsch and T. Schmid are thanked for carrying out the validation experiment at Munich University of Applied Sciences. The authors would also like to acknowledge his collaboration with F. Beyersdorf, T. Doenst, A. Geibel and M. Handke from the Department of Cardiovascular Surgery at the University Hospital, Freiburg, who gave important impulses with their medical advice, and K. Asfaw, S. Hasecic for the manuscript work.

References

- Baccani B., Domenichini F., Pedrizzetti G., 2003. *Model and influence of mitral valve opening during the left ventricular filling*. J. Biomech., **36**, 335-361
- Baccani B., Domenichini F., Pedrizzetti G., 2002. *Vortex dynamics in a model left ventricle during filling*. Eur. J. Mech. B/Fluids, **21**, 527-543
- Baccani B., Domenichini F., Pedrizzetti G., Tonti G., 2002. *Fluid dynamics of the left ventricular filling in dilated cardiomyopathie*. J. Biomech., **35**, **5**, 665-671
- Computational Dynamics Limited, 2003. *StarCD User Guide*. Techn. Report, London.
- Dijkstra E.W., 1959. *A Note on Two Problems in Connexion with Graphs*. Num. Math., **1**, 269-271
- Domenichini F., Pedrizzetti G., Baccani B., 2005 *Three-dimensional filling flow into a model left ventricle*. J. Fluid Mech., **539**, 179-198
- Pedrizzetti G., Domenichini F., 2005. *Nature optimizes the swirling flow in the human left ventricle*. Physical Review Letters., **95**
- Fung Y.C., 1997. *Biomechanics: Circulation*. 2nd edn., Springer-Verlag, Berlin, Heidelberg, New York.
- Guyton A.C., Coleman T.G., Granger H.J., 1972. *Circulation: Overall Regulation*. Ann. Rev. Physiologie, **34**, 13-46
- Handke M., Jahnke C., Heinrichs G., Schlegel J., Vos C., Schmitt D., Bode C., Geibel A., 2003. *New Three-Dimensional Echocardiographic System Using Digital Radiofrequency Data-Visualization and Quantitative Analysis of Aortic Valve Dynamics With High Resolution*. Circulation, **107**, 2876-2879
- Houliind K.C., Sloth E., Oyre S., Kim W.Y., Pedersen E.M., Jorgensen H.S., Hasenkam J.M., 1994 *Three-dimensional visualization of velocity profiles in the human main pulmonary artery with magnetic resonance phase-velocity mapping*. American Heart Journal, **128**, 1130-1138
- Hunter P.J., McCulloch A.D., ter Keurs H.E.D.J., 1998. *Modelling the Mechanical Properties of Cardiac Muscle*. Progr. in Biophysics and Molecular Biology, **69**, 289-331
- Hunter P.J., Nash M.P., Sands G.B., 1996. *Computational Electromechanics of the Heart*. In: Computational Biology of the Heart. Eds. Panfilov A.V., Holden A.V., John Wiley & Sons, Chichester, New York, 345-407
- Hunter P.J., Smaill B.H., Nielsen P.M.F., LeGrice I.J., 1996. *A Mathematical Model of Cardiac Anatomy*. In: Computational Biology of the Heart. Eds. Panfilov A.V., Holden A.V., John Wiley & Sons, Chichester, New York, 171-215
- Jones T.N., Netaxas D.N., 1998. *Patient-specific analysis of left ventricular blood flow*. Computer Science 1496, Springer Verlag, 154-166
- Jung B., 2003. *Private communications*. Department of Cardiovascular Surgery, Universitätsklinikum Freiburg.
- Kilner P.J., Yang G.-Z., Wilkes A.J., Mohiaddin R.H., Firmin D.N., Yacoub M.H., 2000. *Asymmetric redirection of flow through the heart*. Nature, **404**,

- Kim W.Y., Walker P.G., Pedersen E.M., Poulsen J.K., Oyre S., Houliand K., Yoganathan A.P., 1995. *Left ventricular blood flow patterns in normal subjects: A quantitative analysis by three-dimensional magnetic resonance velocity mapping*. JACC, **26**, 224–238
- Lemmon J.D., Yoganathan A.P., 2000. *Three-Dimensional Computational Model of Left Heart Diastolic Function with Fluid-Structure Interaction*. J. of Biomech. Eng., **122**, 109–117
- Liepsch D., Moravec S., Baumgart R., 1992. *Some flow visualization and laser-doppler velocity measurements in a true-to-scale elastic model of a human aortic arch — A new model technique*. Biorheology, **29**, 563–680
- Long Q., Merrifield R., Yang G.-Z., Xu X.Y., Killner P.J., Firmin D.N., 2003. *The influence of inflow boundary conditions on intra left ventricle flow predictions*. J. of Biomech. Eng., **125**, 922–927
- Naujokat E., Kiencke U., 2000. *Neuronal and Hormonal Cardiac Control Processes in a Model of the Human Circulatory System*. Int J. of Bioelectromagnetism, **2**, 2, 1–7
- McQueen D.M., Peskin C.S., 2001. *Heart Simulation by an Immersed Boundary Method with Formal Second Order Accuracy and Reduced Numerical Viscosity*. In: Mechanics for a New Millennium, Proceedings of the 20th ICTAM, Chicago, Illinois. Eds. Aref H., Phillips, J.W., Kluwer Academic Publishers, Dordrecht, Norwell, Massachusetts
- Mortensen E.N., Barrett W.A., 1998. *Interactive Segmentation with Intelligent Scissors*. Graphical Models and Image Processing, **60**, 5, 349–384
- Nakamura M.S., Wada T., Mikami A., Kitabatake, Karino T., 2003. *Computational study on the evolution of an intraventricular vortical flow during early diastole for the interpretation of color m-mode doppler echocardiograms*. Biomech. Model. Mechanobiol., **2**, 1, 59–73
- Nash M.P., Hunter P.J., 2000. *Computational mechanics of the heart*. J. of Elasticity, **61**, 113–141
- Oertel H., 2004. *Biofluid Mechanics of Blood Circulation*. In: Prandtl's Essentials of Fluid Mechanics. Ed. Oertel H., Springer-Verlag, New York, 615–654
- Oertel H., 2005. *Modelling the Human Cardiac Fluid Mechanics*. University Press, Karlsruhe
- Oertel H., Böhle M., Dohrmann U., 2006. *Strömungsmechanik*. 4th edn., Vieweg-Verlag, Wiesbaden
- Oertel H., Laurien E., 2003. *Numerische Strömungsmechanik*. 2nd edn., Vieweg-Verlag, Wiesbaden
- Perktold K., Resch M., Florian H., 1991. *Pulsatile non-Newtonian Flow Characteristics in a Three-dimensional Human Carotid Bifurcation Model*. J. of Biomech. Eng., **113**, 464–475
- Peskin C.S., McQueen D.M., 1997. *Fluid Dynamics of the Heart and its Valves*. In: Case Studies in Mathematical Modeling — Ecology, Physiology, and Cell Biology. Eds. Othmer H.G., Adler F.R., Lewis M.A., Dallon J.C., Prentice-Hall, Englewood Cliffs, New Jersey, 309–337

- Pullan A.J., Buist M.L., Cheng L.K., 2005. *Mathematically modelling the electrical activity of the heart*. World scientific
- Reik M., Meyrowitz G., Schwarz M., Donisi S., Schenkel T., 2005 *A 1D circulation model as boundary condition for a 3D simulation of a pumping human ventricle*. JIFMBE Proceedings, EMBEC 2005, Prague
- Reul H., Talukder N., Mueller E.W., 1981. *Fluid mechanics of the natural mitral valve*. J. of Biomech. Eng., **14**, 14,361–372
- Robb J.S., Robb R.C., 1942. *The normal heart: Anatomy and Physiology of the Structural Units*. Am. Heart J., **23**, 455–467
- Saber N.R., Gosman A.D., Wood N.B., Kilner P.J., Charrier C.L., Firmin D.N.,2001 *Computational flow modeling of the left ventricle based on in vivo mri data: Initial experience*. Ann. Biomed. Eng., **29**, 4, 275–283
- Saber N.R., Gosman A.D., Wood N.B., Merrifield R.D., Yang G.-Z., Charrier C.L., Gatehouse P.D., Firmin D.N.,2003 *Progress towards patient-specific computational flow modeling of the left heart via combination of magnetic resonance imaging with computational fluid dynamics*. Ann. Biomed. Eng., **31**, 1, 42–52
- Schenkel T., Reik M., Malvè M., Markl M., Jung B., Oertel H., 2007 *MRI based CFD analysis of flow in a human left ventricle*. in preparation
- Schmid T., Stock M., Donisi S., Schiller W., Liepsch D., Laschka B., Hirzinger G., Welz A., Oertel H.,2005 *Development and verifikation of ventricle-shaped chambers for the DLR assist device*. Artif. Organs, **28**, 9, 875
- Schwarz R., 2003. *Semiautomatische Segmentierung des linken Herzventrikels für Strömungssimulationen*. Techn. Report, Fraunhofer-Institut für Angewandte Informationstechnik, Sankt Augustin, 1–6
- Walker P.G., Cranney G.B., Grimes R.Y., Delatore J., Rectenwald J., Pohost G.M., Yoganathan A.P.,1996 *Three-dimensional reconstruction of the flow in a human left heart by using magnetic resonance phase velocity encoding*. Ann. Biomed. Eng., **24**, 1, 139–147
- Watanabe H., Hisada T., Sugiura S., Okada J., Fukunari H., 2002. *Computer Simulation of Blood Flow, Left Ventricular Wall Motion and their Interrelationship by Fluid-Structure Interaction Finite Element Method*. JSME, C, **45**, 4, 1003–1012
- Watanabe H., Sugiura H.Sh., Kafuku H., Hisada T.S., 2004. *Multiphysics simulation of left ventricular filling dynamics using fluid-structure interaction finite element method*. Biophysical J., **87**, 2074–2085

ISBN-13: 978-3-86644-087-6

ISBN-10: 3-86644-087-1

www.uvka.de